Systematic Geolocation Errors of FengYun-3D MERSI-II

Hongbo Pan, *Member, IEEE*, Zehua Cui, Xiuqing Hu, and Xiaoyong Zhu

***Abstract*— Geolocation accuracy is a critical issue for remote sensing applications. To achieve subpixel accuracy, geolocation errors need to be systematically identified and corrected. In this study, we propose a geometric sensor model for FengYun-3D (FY-3D) MERSI-II, a second-generation visible (VIS)/infrared (IR) spectroradiometer, to generate the geolocation lookup table (GLT). The geometric sensor model retrieves the imaging rays from the focal plane to the K-mirrors, 45° scanning mirrors, the platform, and the earth's surface. After refining the attitude errors with ground control points (GCPs), the rigorous sensor model can achieve subpixel geolocation accuracy. However, significant systematic geolocation errors were identified from the residuals, especially for the area with large view angles. To study the errors of MERSI-II, we proposed a homogenous coordinate in the focal plane. As proven by both theory and experiments, the attitudes were adjusted to a wrong value and introduced systematic errors when there were principal point errors. The pitch angle error of K-mirrors caused the oscillation in the flight direction. The principal distance error introduced line coordinate-related error in the flight direction. Meanwhile, the initial phase angle error between the K-mirror and 45° scanning mirrors caused the line coordinate-related errors in the scanning direction. After correcting all the above-mentioned errors, the systematic geolocation errors of MERSI-II were removed. With 23 independent datasets, the root mean square errors (RMSEs) of 250 m bands were approximately 0.4 pixels, 100 m at nadir.**

***Index Terms*— Geolocation, geometric sensor model, medium resolution spectrum imager-II (MERSI-II).**

I. Introduction

THE medium resolution spectrum imager-II (MERSI-II) is the new generation payload of Chinese polar-orbiting meteorological satellites, which was adopted in FengYun-3D (FY-3D). The follow-up mission, FengYun-3E, was launched in July 5, 2021, on an early-morning orbit. MERSI-2 is a 25-channel VIS/infrared (IR) spectroradiometer, replacing and merging MERSI-I [1] and visible and infra-red radiometer (VIRR) of FY-3A/3B/3C [2]. The ground distance of instant field of view (IFOV) of six channels is 250 m at nadir, while the ground distance of the rest of the 19 channels is 1000 m [3]. The MERSI-II captures the image of approximately 2900 km swath with a single scan from an 830 km orbit height. And 23 types of global information products daily were generated by ground application system [3].

The geolocation procedure is a fundamental preprocessing step. It generates the level 1B product from the geolocation lookup table (GLT). This geolocation information can additionally be used to combine the multisensor, multitemporal remote sensing data, as well as analyze quantitative physical and chemical information about land, ocean, and atmosphere [4], [5].

Much effort was devoted to developing subpixel geolocation methods for whiskbroom cameras, like Advanced Very High Resolution Radiometer (AVHRR) [6], [7], Moderate-Resolution Imaging Spectroradiometer (MODIS) [8], [9] and Visible Infrared Imaging Radiometer Suite (VIIRS) of Suomi National Polar-orbiting Partnership (SNPP) and Join Polar Satellite System (JPSS) [10]–[12]. In the early era of development of these methods, both ephemeris and attitude should be estimated for satellite navigation. With the improvement of ephemeris accuracy, only attitude needs to be refined for AVHRR [6], [13]. Recently, several studies also reported that the compensation for attitude can achieve subpixels geolocation accuracy for FY-3D's microwave radiation imager (MWRI), whose spatial resolution is approximately 5–6 km [14], [15]. For MERSI of FY-3A, the geolocation accuracy can achieve approximately 2 pixels for 250 m bands, after compensating for the boresight bias via several ground control points (GCPs) at the coastline [16]. The MERSI-II of FY-3D achieved similar geolocation accuracy in the object space for 1000 m bands, when the images of Landsat-8 Operational Land Imager (OLI) are used as reference images [17].

In general, there are two ways to analyze the geolocation errors for whiskbroom cameras: in the object space and the image space. In the first case, the whiskbroom image would be rectified in a specific projection, and the image correlation would be used to extract high-precision GCPs from higher accurate reference images [9], [18]. The absolute geolocation accuracy is determined in the specified projection. However, the ground sample distance (GSD) of the whiskbroom camera changes with the distance between the satellite and the object. Therefore, the geolocation errors in the object space depend on the view angles. Additionally, map projection on an area of over 2900 km is prone to distortion owing to the difficulty

Manuscript received September 18, 2021; revised January 7, 2022 and February 5, 2022; accepted March 2, 2022. Date of publication March 4, 2022; date of current version April 5, 2022. This work was supported in part by the National Key Research and Development Program of China under Grant 2018YFB0504905, in part by the National Natural Science Foundation of China (NSFC) Project under Grant 41971418, and in part by the Gaofen Satellite Remote Sensing Surveying and Mapping Application Demonstration System (Phase II) of China under Grant 42-Y30B04-9001-19/21. *(Corresponding author: Hongbo Pan.)*

Hongbo Pan and Zehua Cui are with the School of Geosciences and Info-Physics, Central South University, Changsha 410083, China (e-mail: hongbopan@csu.edu.cn; czh1997@csu.edu.cn).

Xiuqing Hu is with the Key Laboratory of Radiometric Calibration and Validation for Environmental Satellites, China Meteorological Administration, National Satellite Meteorological Center, Beijing 100081, China (e-mail: huxq@cma.gov.cn).

Xiaoyong Zhu is with the Land Satellite Remote Sensing Application Center, Ministry of Natural Resources, Beijing 100048, China (e-mail: whuzhu@qq.com).

Digital Object Identifier 10.1109/TGRS.2022.3156999

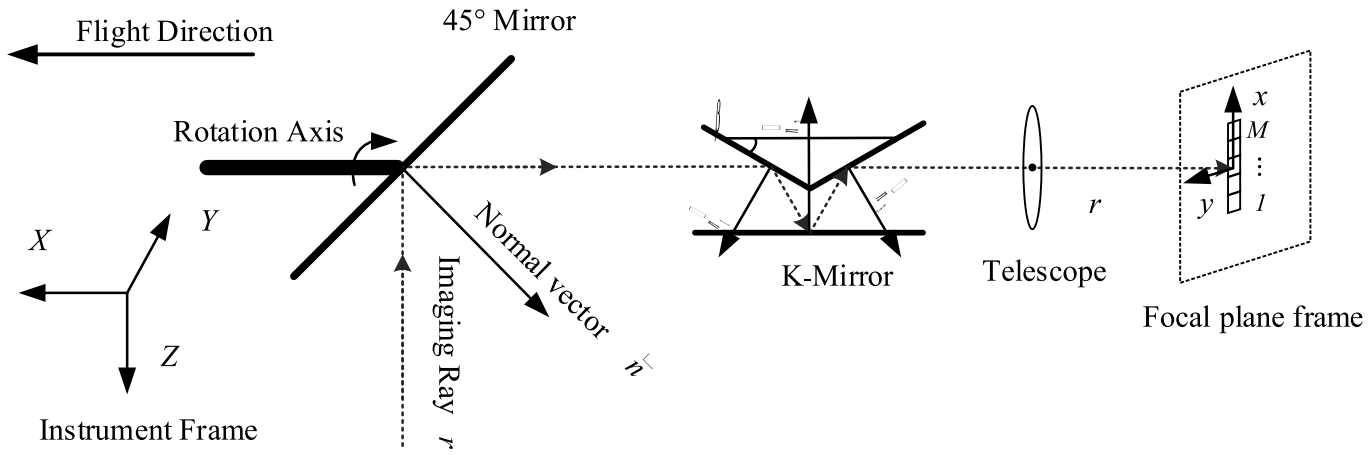

Fig. 1. Sketch of MERSI-II.

of choosing an appropriate map projection. Past research has tried to reproject the object coordinate to the image space to determine the errors in the image space [13], [19], because the geolocation errors introduced by sensors or platform depend on the imaging geometry. Schmidt *et al.* [19] found that there were view zenith angle (VZA) related geolocation errors. And the geolocation errors increased with view angle for MERSI-II 1000 m bands [17].

To improve the geolocation accuracy, a more comprehensive investigation on the error sources is required, similar to the MODIS [9], [20]. Due to the very small field of view (FoV), these errors were correlated. More than that, there is a unique equipment, K-mirror, in MERSI-II to correct the image rotations [21]. In this article, a rigorous sensor model was developed for geolocation of MERSI-II. To analyze systematic errors, a homogenous coordinate in the focal plane was proposed.

Section II presents the geometric sensor model for MERSI-II, including detailed MERSI-II design, the transformation of imaging rays, and geolocation. Section III proposed a new homogenous coordinate in the focal plane to analyze geolocation errors related to sensors, platforms, and targets. A dataset was used to explore the properties of geolocation errors for FY-3D MERSI-II. A summary appears in Section V.

II. Geometric Sensor Model for MERSI-II

The geometric sensor model describes the relationship between the image coordinate and spatial coordinate of target, which is used to calculate the GLT. In general, the geolocation can be described as the line of sight (LoS), retrieved from image coordinate, which intersects with the earth's surface for the geodetic coordinate.

A. Medium Resolution Spectrum Imager-II

The MERSI-II utilizes a 45° scanning mirror to capture ground images in the across-track direction. However, the mirror would introduce misalignment of image rotation for those sensors with multidetectors, like MERSI-II. To correct this image rotation, a K-mirror with three reflectors was adopted since FY-3A [21]. After many reflections, the light would be focused by telescope and projected to the focal plane, as illustrated in Fig. 1. To analyze the imaging geometry, an instrument frame system was introduced, whose X-axis is the rotation axis of 45° scanning mirror, Z-axis points to the center of earth view angle and Y-axis is determined by right-hand rule.

The 45° scanning mirror was named by the 45° angle between rotation axis and normal vector of reflective mirror. To scan the across-track direction, the rotation axis parallels the flight direction. The mirror makes a round in 1.5 s, capturing a frame about 10 km in the nadir. The center of the earth view angle points to the nadir.

The K-mirror is composed of three reflectors. The normal vector of the second mirror is perpendicular to the rotation axis, while angles of first and the third mirrors between the normal vector and rotation axis are equal to β. The rotation axis of the K-mirror is designed the same as 45° scanning mirror. The rotation velocity of the K-mirror is half as 45° scanning mirror, 20 rounds/min. The normal vector of the second mirror points to $-Z$-direction of the instrument frame, when the 45° scanning mirror points to the nadir.

After being separated by four dichromic beam splitters, the collected radiation was projected to five focal plane assemblies (FPAs) for five spectral intervals, including visible (VIS), visible and near-infrared (VNIR), short-wave infrared (SWIR), mid and long-wave infrared (MLWIR), and long-wave infrared (LWIR), as illustrated in Fig. 2. There were two types of linear multi detectors, 40 detectors with 0.3 mrad for 250 m bands and ten detectors with 1.2 mrad for 1000 m bands. The linear detectors are perpendicular to the scanning direction in the FPAs. In the focal plane frame, the x-axis is opposite to the flight direction, while the y-axis is determined by right-hand rule. After correcting the image rotation by K-mirror, all bands were co-registered to the reference band by a simple shift in the scanning direction. Therefore, the geolocation of MERSI-II is carried out for the reference band.

B. Geometric Sensor Model

For the dynamic imaging system, both the imaging ray and the imaging time are important. With the rows in the image

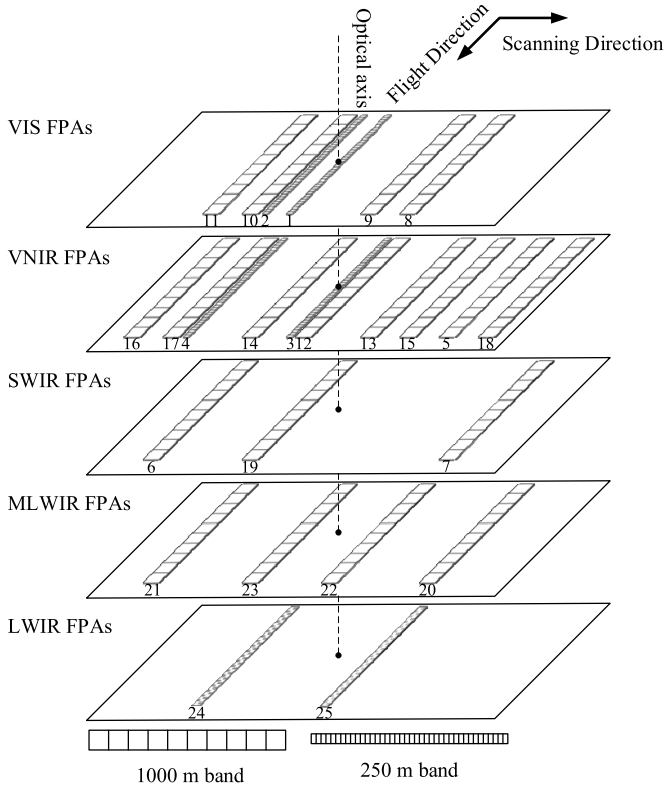

Fig. 2. FPAs of MERSI-II.

coordinate and the number of detectors M, the pixels (r, c) can determine the corresponding frame N and the corresponding detector r_N in the frame. Then, the coordinate (x, y) in the focal plane frame is

$$\begin{cases} x = \left(r_N - \dfrac{M}{2}\right) \cdot \mu + x_0 \\ y = y_0 \end{cases} \tag{1}$$

where μ indicates the pixel spacing of detectors and (x_0, y_0) is the central point of the linear charge-coupled device (CCD) in the focal plane.

Getting the imaging ray in the telescope requires two steps: retrieving 3-D imaging rays in the camera $\begin{bmatrix} X & Y & Z \end{bmatrix}_c^T$ with principal distance f from 2-D image points as

$$\begin{bmatrix} X \\ Y \\ Z \end{bmatrix}_c = \begin{bmatrix} x \\ y \\ -f \end{bmatrix} \tag{2}$$

and changing the coordinate to the instrument frame with transformation matrix $\mathbf{R}_c^{\text{tel}}$

$$\mathbf{R}_c^{\text{tel}} = \begin{bmatrix} 0 & 0 & 1 \\ 0 & 1 & 0 \\ -1 & 0 & 0 \end{bmatrix}. \tag{3}$$

Because of the rotation of K-mirror and 45° scanning mirror, the scan angle θ depends on the time t. The detectors of 1000 m bands sample at an interval of t_0 which is 224 μs, while the sample frequency of 250 m bands is four times that of the 1000 m bands. Within 0.4587 s, the 45° scanning mirrors scan the earth view from –55.04° to 55.04° with velocity $\dot{\theta}$ which is 4.189 rad/s. For a 1000 m band, the angle interval of adjacent columns is 0.94 mrad, smaller than the IFOV. Let θ equal 0, when the sample c is at the center of the image. Then scan angle is defined as

$$\theta = \left(c - \frac{W}{2}\right) \cdot t_0 \cdot \dot{\theta} \tag{4}$$

where W is the width of the image, and t_0 is the dwell time, which is different for 1000 m bands and 250 m bands.

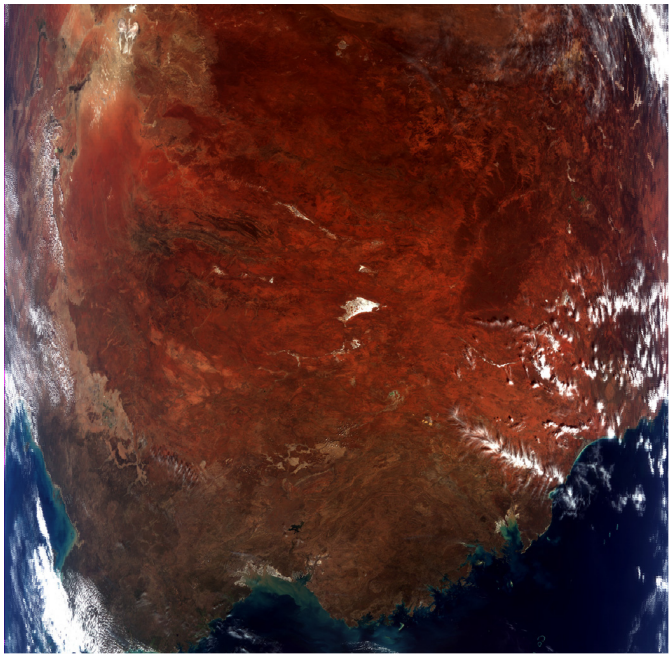

Fig. 3. MERSI-II dataset covering Australia with few clouds.

According to (19), the reflection matrix of K-mirror is independent of the angle β. More details about the reflection matrix of 45° scanning mirror and K-mirror can be found in Appendix A. Using (18), the rotated reflection matrix of K-mirror is

$$R_k(\theta/2) = \begin{bmatrix} 1 & 0 & 0 \\ 0 & \cos\theta & \sin\theta \\ 0 & \sin\theta & -\cos\theta \end{bmatrix}. \tag{5}$$

In the nadir view, the normal vector of 45° scanning mirror is $\vec{n} = \begin{bmatrix} -1/\sqrt{2} & 0 & 1/\sqrt{2} \end{bmatrix}^T$ in the instrument frame. And the reflection matrix of 45° scanning matrix is

$$R_m(\theta) = \begin{bmatrix} 0 & -\sin\theta & \cos\theta \\ -\sin\theta & \cos^2\theta & \sin\theta \cdot \cos\theta \\ \cos\theta & \sin\theta \cdot \cos\theta & \sin^2\theta \end{bmatrix}. \tag{6}$$

Combine the K-mirror and 45° scanning mirror, the transformation matrix of scan assemblies is

$$R_{\text{mkt}} = R_m(\theta) \cdot R_k(\theta/2) \cdot \mathbf{R}_c^{\text{tel}} = \begin{bmatrix} 1 & 0 & 0 \\ 0 & \cos\theta & -\sin\theta \\ 0 & \sin\theta & \cos\theta \end{bmatrix}. \tag{7}$$

And the LoS in the body system is

$$\begin{bmatrix} X \\ Y \\ Z \end{bmatrix}_b = R_{\text{mkt}} \cdot \begin{bmatrix} X \\ Y \\ Z \end{bmatrix}_c = \begin{bmatrix} x \\ y \cdot \cos\theta + f \cdot \sin\theta \\ y \cdot \sin\theta - f \cdot \cos\theta \end{bmatrix}. \tag{8}$$

According to (7), the K-mirror compensates for the image rotation with its multidetectors, because the transformed ray in X-direction is independent of scan angle θ.

The attitude and orbit determination system also provides crucial attitudes for geolocation. Global positioning system (GPS) receiver was adopted to determine the position $\begin{bmatrix} X_S & Y_S & Z_S \end{bmatrix}^T$ of FY-3D satellite. There are two types of attitudes for FY-3D. The first describes the transformation $\mathbf{R}_{\text{body}}^{O}$ with Euler angles between the satellite body coordinate and orbit coordinate. With the position and velocity in the earth-centered inertial (ECI) coordinate, the transformation matrix $\mathbf{R}_{O}^{\text{ECI}}$ from orbit coordinate to the ECI coordinate can be calculated. The second are the quaternions, indicating the transformation matrix between navigation system and ECI. In this case, the boresight alignment of the navigation system would need to be considered. Both attitudes can calculate the transformation matrix $\mathbf{R}_{\text{body}}^{\text{ECI}}$. The LoS in the ECI can be transformed to earth-centered earth-fixed (ECEF) coordinate by IERS conventions [22].

With above transformation, the LoS of each pixel in the ECEF is

$$\begin{bmatrix} X \\ Y \\ Z \end{bmatrix}_{\text{ECEF}} = \begin{bmatrix} X_S \\ Y_S \\ Z_S \end{bmatrix} + m \cdot \mathbf{R}_{\text{ECI}}^{\text{ECEF}} \cdot \mathbf{R}_{\text{body}}^{\text{ECI}} \cdot \mathbf{R}_{\text{mkt}} \cdot \begin{bmatrix} x \\ y \\ -f \end{bmatrix} \tag{9}$$

where m is scale factor.

C. Geolocation

The retrieved ray would intersect with the earth's surface to determine the scale factor m and calculate the Cartesian coordinate in the ECEF. Due to the varying view angle, the topographic relief introduces disparity in the image. Therefore, a 7.5-arc-second spatial resolution global digital elevation model (DEM), GMTED2010 [23], was used to determine topographic surface. To avoid divergence as well as any occlusion-induced problem, the ray-tracing method is preferred as it determines the intersection in a fixed elevation interval.

Transforming the Cartesian coordinate to the geodetic coordinate can be expressed as the solution of a quartic equation [24]. To achieve a better computation efficiency and accuracy, the iterative method is applied [25]. After intersection and coordinate transformation, a GLT for each pixel could be built for MERSI-II.

III. Systematic Errors in Focal Plane

The sources of geolocation errors common with the MERSI-II can be classified into three categories: the sensors, the platforms, and the targets [26]. Ideally, the geometric sensor model can be described by (9). However, due to the imperfect assemblies and the varieties of space environments, these errors need to be taken into consideration. Some past studies have preferred to categorize the geolocation errors according to frequency [20]. Certainly, the frequency of geolocation errors is an important indicator because different error sources would introduce geolocation errors with different frequencies.

Due to the very small FoV and highly dynamic imaging system, the errors of MERSI-II are correlated. For example, the roll angle error of a platform cannot be distinguished from the principal point errors y_0 in the focal plane. Time errors and scan errors introduce the similar geolocation errors. It is difficult to calculate the image coordinate (r, c) from the object coordinate with geometric sensor model.

According to Section II-B, each pixel defines the LoS, which has one freedom. To analyze the systematic errors of MERSI-II, the homogenous coordinate $\begin{pmatrix} p_x & p_y & f/\mu \end{pmatrix}$ in the focal plane is introduced, which is defined as

$$\begin{bmatrix} p_x \\ p_y \\ \dfrac{f}{\mu} \end{bmatrix} \equiv \frac{f}{\mu} \cdot \begin{bmatrix} \dfrac{X_c}{Z_c} \\ \dfrac{Y_c}{Z_c} \\ 1 \end{bmatrix}. \tag{10}$$

The units of (p_x, p_y) are pixels, and 1 pixel equal to one IFOV. Considering the smaller dwell angle in the scanning direction, the spatial resolution of p_y is lower than the real image space. Nevertheless, the p_x is in the flight direction and the p_y in the scanning direction, which were counterintuitive.

A. Errors of MERSI-II

According to Fig. 1, the errors of MERSI-II can be further divided into three different assemblies, including the telescope with focal plane, the K-mirror and the 45° scanning mirror.

The principal distance f and principal points are interior orientation parameters. However, the principal point error can be absorbed by the deployment parameters (x_0, y_0) of (1). According to (8), the $y = y_0$ is correlated with the scanning angle θ, which relies on the sample coordinate c. In most cases, the y_0 is calibrated by band-to-band registration. For the sake of simplicity, let $y_0 = 0$, then the Δx_0 cause the errors in Δp_x as $\Delta p_x = \Delta x_0/\mu$. And the errors of principal distance f would introduce normalized line coordinate r_N related errors in Δp_x, which is

$$\Delta p_x = \frac{\Delta f}{f + \Delta f} \cdot \frac{x}{\mu}. \tag{11}$$

The major error of K-mirror is boresight misalignment. The misalignment of K-mirror can be represented with three angles the ϕ with X-axis, the α with Y-axis and γ with Z-axis. As shown in Appendix B, γ has no impact on the geolocation. α indicates the pitch angle of K-mirror. ϕ represents the initial phase angle between the K-mirror and 45° scanning mirror, and can be directly summed with scanning angle $\theta/2$. Given the boresight misalignment, the reflection matrix of K-mirror is derived as (22).

The boresight misalignment of the 45° scanning mirror can be absorbed by attitude errors, which will be discussed in Section IV. However, two other error sources should be considered: the scanning angle $45° + \tau$ and the scanning errors. The former would introduce the similar errors as principal distance f, as demonstrated in Appendix C. The latter is caused by variation of rotation velocity of the scanning mirrors and causes the scanning angle $\theta/2$ to not be linearly correlated

with time t. It can be modeled by a sum of the sinusoidal functions

$$\theta(t) = \sum_{i=1}^{n} a_i \sin(\omega_i \cdot t + \phi_i) \tag{12}$$

where a_i, ω_i and ϕ_i $(i = 1, 2, \ldots, n)$ are the amplitude, angular frequency and phase, respectively.

B. Errors of Platform

The errors of platform are consisted of position error and attitude error. Since the GPS receivers were used to determine the ephemeris of meteorological satellites, the position accuracy of satellites can achieve meters even without precise orbit, which can meet the requirement of geolocation. The attitude error is the major error source causing geolocation errors.

Two types of errors can be modeled by attitude errors, including the errors of attitude determination and the misalignment between navigation system and the whiskbroom cameras. Generally, the former is regarded as stable and can be compensated by a rotation matrix between $\mathbf{R}^{O}_{\text{body}}$ and $\mathbf{R}_{\text{mkt}}$, whereas the latter changes with time and can be modeled by attitudes of $\mathbf{R}^{O}_{\text{body}}$. In practice, there is no significant difference between above two errors.

The attitude errors can be modeled by three Euler angles, the roll angle $\Delta\omega$, the pitch angle $\Delta\varphi$, and yaw angle $\Delta\kappa$. These errors would introduce geolocation errors in focal plane, as shown in Appendix D

$$\begin{cases} \Delta p_x = \left(\dfrac{f}{\mu} + \dfrac{x^2}{\mu \cdot f}\right) \cdot \cos\theta \cdot \Delta\varphi - \left(\dfrac{f}{\mu} + \dfrac{x^2}{\mu \cdot f}\right) \\ \qquad \cdot \sin\theta \cdot \Delta\kappa \\ \Delta p_y = \dfrac{x}{\mu} \cdot \sin\theta \cdot \Delta\varphi + \dfrac{f}{\mu} \cdot \Delta\omega + \dfrac{x}{\mu} \cdot \cos\theta \cdot \Delta\kappa. \end{cases} \tag{13}$$

For MERSI-II, the maximum of x/f is the half FoV, about 5/830, and the maximum of x/μ is 20 for 250 m bands. Therefore, the errors with coefficients f/μ are the major errors. The pitch angle error $\Delta\varphi$ introduce the cosine curves error in the flight direction Δp_x and small sine curves error in the scan direction Δp_y. The roll angle error $\Delta\omega$ causes the shift in the scan direction, as same as initial scanning angle. And the yaw angle error $\Delta\kappa$ causes the geolocation errors in the flight direction as sinusoids about scanning angle, and cosine curves in the scanning direction. It is worth noting that x/μ is related to the line number, that is, the errors with coefficients x/μ would change with r_N and view angle θ, and are not negligible as AVHRR [27].

C. Errors of Targets

The errors of targets are atmospheric refraction, light aberration, and elevation errors. The atmospheric refraction would cause the departure of view angle about 11 mrad at the 70° apparent zenith distance. This error can be ignored, because the minimum IFOV is 236 mrad. Due to the lower resolution, the light aberration is also not significant. The elevation errors of target come from the elevation error of DEM and the planimetric error of geolocation. The GMTED2010 root mean square errors (RMSEs) at 7.5 arc-seconds resolution range between 26 and 30 m, which is sufficient for MERSI-II geolocation [23].

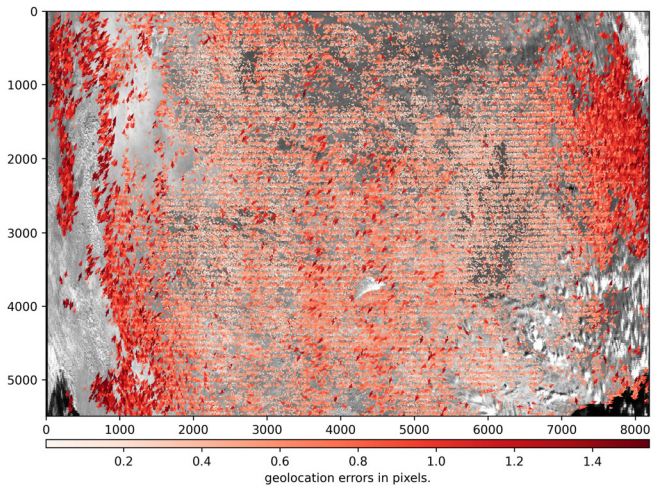

Fig. 4. Geolocation errors of MERSI-II 250 m bands in the focal plane.

IV. Experiments and Discussions

A. Datasets

The MERSI-II data of FY-3D is freely available from the National Satellite Meteorological Center. The level 1 250 m resolution data contain six 250 m bands earth view data after co-registration and a GLT with 20 pixels interval. Each file is partitioned with 5 min interval and in hierarchical data format (HDF5), resulting the image size with 8192 pixels in columns and 8000 pixels in rows. Nevertheless, a separated GLT file (named as GEOQK) is also provided, which include latitude and longitude for each pixel. During the geolocation processing, the ephemeris, attitudes, and time information are required, which are stored in the onboard calibrator (OBC) file.

To evaluate the geolocation accuracy, the datasets capturing the lands without cloud are preferred. Therefore, the dataset, FY3D_MERSI_GBAL_L1_20200517_0505_0250M_MS, was adopted, as shown in Fig. 3. The denoted the imaging time for 20200517_0505 was May 17, 2020 5:05, which was unique and used to indicate the dataset. Given the high signal-to-noise ratio (SNR), the reflective solar band 4 (named as RefSB4 with 0.865 μm center wavelength) was used to extract GCPs.

The eighth band of Sentinel-2 multispectral instrument (MSI), central wavelength 832.8 nm, served as the cloud-free reference images via google earth engine. The geolocation accuracy of MSI nonrefined L1C products is about 10 m at 94.45% confidence [28]. The spatial resolution of reference images was degraded to 240 m via averaging pixel values, slightly better than the spatial resolution of MERSI-II nadir images. However, the GSD of MERSI-II changes significantly with the view angle, resulting in panchromatic distortions of the original images. To reduce the impact of geometric distortions, the reference images were used to simulate a new reference image with GLT. After that, the RefSB4 of MERSI-II was matched with simulated images. The normalized cross

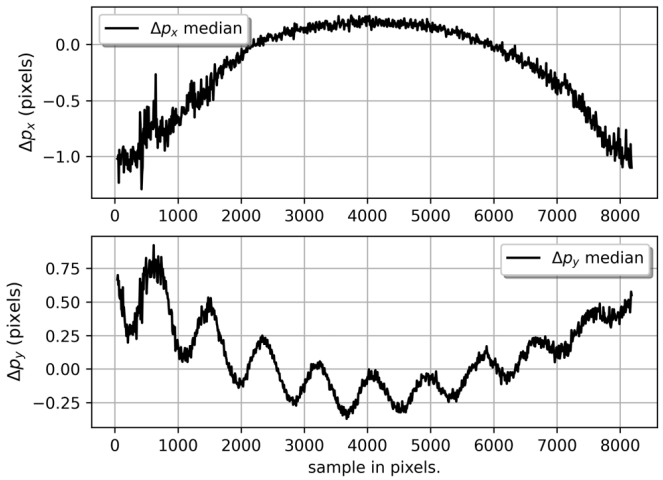

Fig. 5. Median residuals of Δp_x and Δp_y with sample coordinates.

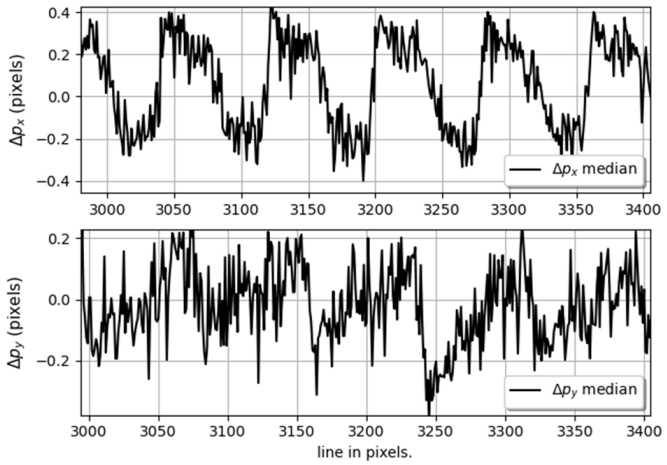

Fig. 6. Medians residuals of Δp_x and Δp_y with line coordinates.

correlation algorithm is used to find the initial corresponding points, then the coordinates of conjunctive points were refined by the least square matching (LSM), which can achieve subpixel accuracy. The matching window is 11×11 pixels, keeping a balance between matching accuracy and details of errors. The outliers were removed by Guided Locality Preserving Feature Matching (GLPM) [29], and there were over 100 000 GCPs left.

B. Attitude Errors of FY3D MERSI-II

The design parameters were adopted to retrieve the LoS of MERSI-II. For dataset 20200517_0505, only Euler angles were available. Given that the attitudes of FY-3D are usually small and contain random Euler angle errors, the average attitude of the entire scene was adopted. Fifth-degree polynomials were used to build the orbit model. The GCPs were used to estimate the boresight misalignment to refine the geometric sensor model.

With (10), both object coordinate (*lat, lon, h*) and image coordinate (*r, c*) can be transformed to the focal plane to obtain two coordinates. The difference $\left(\Delta p_x, \Delta p_y\right)$ between two coordinates indicates the geolocation errors. The geolocation residuals are shown in Fig. 4, in which the color indicates the magnitude of the errors, and the arrows show the direction. To make the geolocation errors consistent with the image coordinates, p_x is plotted in the line direction and p_y in the sample direction. The RMSEs of $(p_x,\ p_y)$ are 0.50 pixels, slightly better than the true RMSEs 0.52 pixels in the image space. This is mainly because the IFOV is slightly larger than the angle between adjoint pixels.

The GLT of view angles –27° to 40° can achieve subpixel accuracy. However, there were significant systematic errors pointing to top-right direction with larger view angles. To illustrate these systematic errors, the median residuals of every eight columns were calculated and plotted with sample coordinate in Fig. 5. The Δp_x reduced from 0.2 to –1.0 pixels in the cosine curve way when the view angle increased with the sample coordinate. According to (13), such errors can be absorbed or introduced by $\Delta\varphi$. The $\Delta\varphi$ might be adjusted to an inaccurate value if there were other errors. Nevertheless, there were significant fringes in both sample and line directions, as illustrated in Fig. 4. The fringes in the sample direction also can be identified from Fig. 5. The Δp_y was from –0.27 to 0.75 pixels. To the best of our knowledge, the periodic fringes in the scan direction can be caused by the unsteady scanning of 45° scanning mirrors or K-mirrors. The maximum magnitude of fringes was approximately 0.4 pixels, and reduced with the sample coordinate. The frequency of such periodic errors was approximately 20 Hz.

The fringes in the line direction are a unique phenomenon to the MERSI. To highlight the fringes, the median residuals of line 3000–3400 were zoomed in, as illustrated in Fig. 6. The median of Δp_x oscillated with line number. The frequency was 80 pixels, the same as K-mirror. And the magnitude of such frame is about 0.2 pixels. Considering the scanning geometry of K-mirrors, the misalignment in pitch angle might introduce such errors. In the first period of 45° scanning mirrors, the pitch angle of K-mirrors would cause the LoS to point up as in Fig. 1. The K-mirrors would point down, when the 45° scanning mirrors rotate to the same positions in the following rounds.

There were periodic skews in the Δp_y, whose frequency is equal to the Δp_x. As discussed in Section III, such kind of errors can be introduced by attitude errors or the errors of MERSI-II, such as the initial phase angle errors of K-mirrors, principal distance errors.

C. Systematic Errors of MERSI-II

To elaborate the properties of MERSI-II errors, different parameters were tested to illustrate the impact on the geolocation accuracy. Given the systematic errors, the central point error in the CCD direction Δx_0, the pitch angle error α of K-mirror and the principal distance f were further studied. The GCPs were used to verify the geolocation accuracy.

According to the errors of Δp_x, Δx_0 was set to $-\mu$, -2μ, -3μ, and the medians of Δp_x were calculated with or without attitude compensation. The RMSEs increased from 0.50 pixels to 1.1, 2.0, and 3.0 pixels, when the same attitude compensation model was adopted. The median Δp_x were

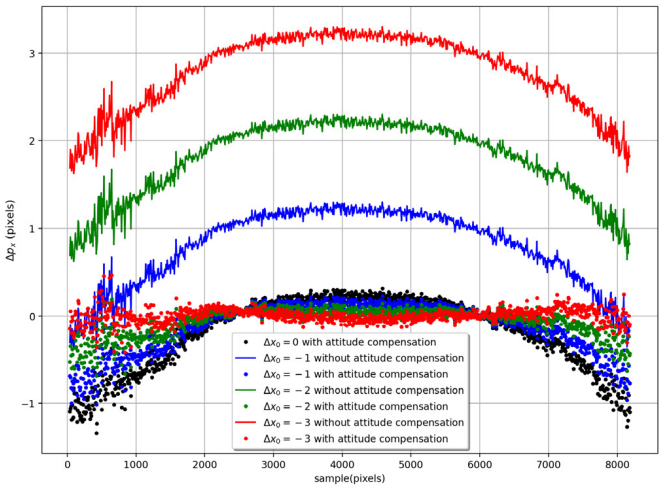

Fig. 7. Median Δp_x with the sample coordinate for different Δx_0.

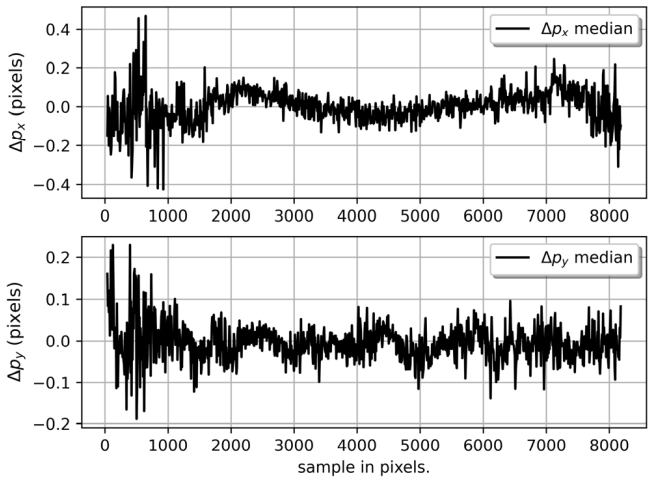

Fig. 8. Median residuals of Δp_x and Δp_y after adjusting Δx_0 and scanning angles.

almost synchronously increasing with Δx_0, as shown in Fig. 7. However, the curvatures of the Δp_x reduced with the Δx_0, when attitude compensation was adopted to correct attitude errors. After compensating for the attitude, the RMSEs were 0.50, 0.46, 0.43, and 0.42 pixels, at 0, $-\mu$, -2μ, and -3μ, respectively. The attitudes were adjusted to an incorrect value, introducing Δp_x as cosine curves, if there were interior orientation parameters errors. After adjusting the Δx_0 to -3μ, the median of Δp_x was around 0 pixels, as shown in Fig. 8.

The oscillation of Δp_y can be modeled by rotation velocity of the scanning mirrors, as (12). Considering the stabilization of machinery and electronics, the sum of sines with six sets of parameters were used to model the oscillation. And the scanning angle table with time is established for scanning angle interpolation. After compensating for the uneven scanning errors of 45° scanning mirrors, the median residuals were calculated with sample coordinate, as shown in Fig. 8. The noise of the first 1000 pixels was larger than the rest, because the GCPs were sparser and influenced by clouds.

With (22), the pitch angle errors $\Delta\alpha$ of K-mirrors would cause the two times errors in the focal plane. After adjusting

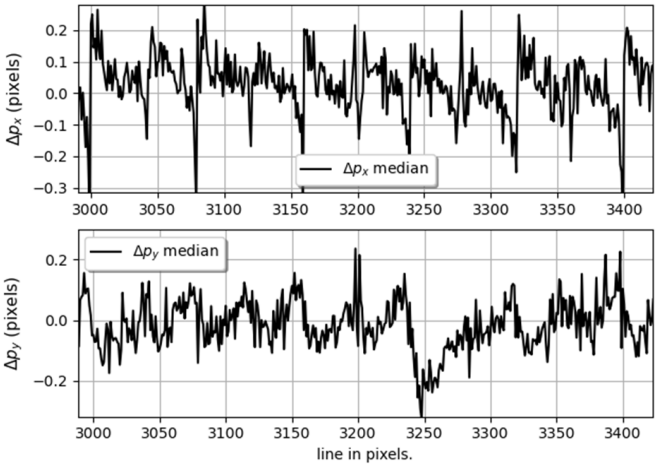

Fig. 9. Residuals with K-mirror pitch angle correction.

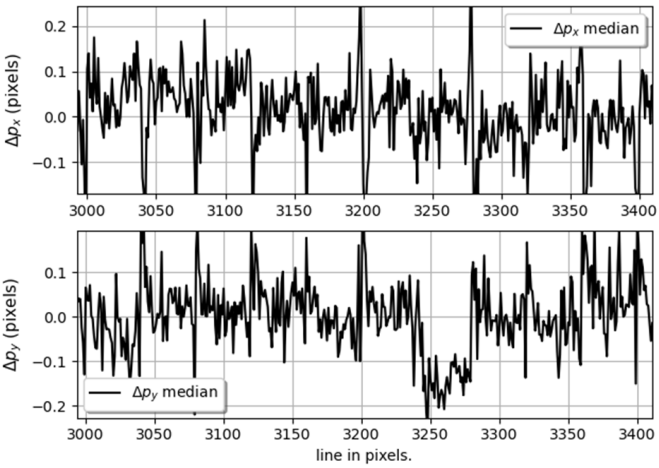

Fig. 10. Residuals with principal distance and initial phase angle correction.

the $\Delta\alpha$ to –0.1 IFOV, the significant oscillation of Δp_x between the adjacent frames were removed, as shown in Fig. 9. Nevertheless, there were pulses for each 40 pixels, as the same as frame height. The bow tie phenomenon of whiskbroom cameras introduces such errors because the matching windows would contain the pixels of adjacent frame, which is suffering from geometric distortions. It is difficult to extract highly accurate GCPs for discontinuous images, which have large gradients at the edges of frames. Compared with Fig. 6, the oscillation in the scanning direction was also reduced.

In each frame, there were skews in both flight and scanning direction. The principal distance error Δf would cause the skews in the flight direction, as proved in (11). From Fig. 9, approximately from 0.1 to –0.1 pixels skew can be identified. Therefore, the principal distance error is about $f/200$. The skews in the scan direction are not very significant, approximately from –0.1 to 0.1 pixels for the first six frames. With the frame size $M = 40$, the initial phase angle is about –0.1/40. After correcting the principal distance and initial phase angle, there were no systematic skews in Fig. 10.

After compensating for the systematic errors, the Δp_x and Δp_y were recalculated with GCPs. The RMSEs were reduced to 0.32 pixels. As shown in Fig. 11, there were then no

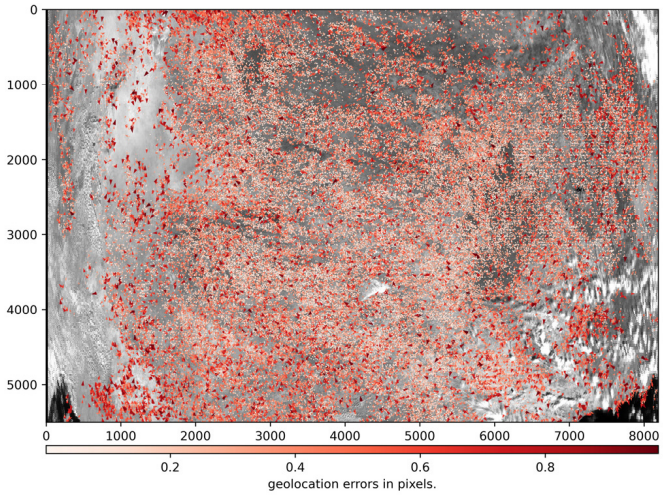

Fig. 11. Geolocation errors of MERSI-II after compensating for systematic errors.

systematic errors but many gross errors, whose residuals were much larger than those of their neighbors.

D. Geolocations of MERSI-II

Due to the limited accuracy of attitudes in the OBC file, the average attitudes need to be refined with GCPs. Meanwhile, the geometric parameters might change with time. To validate the geometric model, 23 datasets, covering Asia, Africa, Europe, and Australia over one year, were used in four schemes experiments.

1) *Scheme 1 (S1):* Geolocation with parameters of dataset 20200517_0505, not refining attitudes.
2) *Scheme 2 (S2):* Geolocation with three different sets of parameters: 20200517_0505, 20210111_1315, and 20210620_1100, not refining attitudes.
3) *Scheme 3 (S3):* Geolocation with parameters of dataset 20200517_0505, refining attitudes.
4) *Scheme 4 (S4):* Geolocation with three different sets of parameters: 20200517_0505, 20210111_1315, and 20210620_1100, refining attitudes.

For the majority of datasets, the number of GCPs were over 80 000. And the rest were covered a lot of featureless area, such as deserts, clouds, and oceans. The GCPs were distributed evenly in the whole scenes.

The RMSEs were calculated for each scheme as illustrated in Table I. In spite of only one geometric calibration, the RMSEs for S1 were within 2 pixels. The geolocation accuracy was not improved by the geometric calibration of dataset 20210111_1315 and dataset 20210620_1100, since the attitude errors of OBC file were random. The RMSEs for S2 were within 1 km, achieving subpixels geolocation accuracy for 1000 m bands. After refining attitudes with GCPs, the RMSEs for S3 were time dependent. For the datasets of May 2020, the RMSEs were approximately 0.4 pixels. In the case of 20200513_1320, the RMSEs were 0.55 pixels, because the attitudes changed with time and the mean attitudes were not sufficient to guarantee the highly accurate geolocation. After six months or more time operation, the geometric parameters varied, especially the pitch angle of K-mirrors, which introduced more significant oscillations than Fig. 6. After estimating the geometric parameters, the RMSEs for S4 were approximately 0.4 pixels.

TABLE I
GEOLOCATION ACCURACY OF FY-3D MERSI-II FOR FOUR SCHEMES

Datasets	Number of GCPs	RMSE (pixels)			
		S1	S2	S3	S4
20200504_1110	122827	1.10	1.10	0.36	0.36
20200504_1250	144129	0.89	0.89	0.46	0.46
20200508_1135	119000	1.20	1.20	0.38	0.38
20200509_1255	109911	1.48	1.48	0.42	0.42
20200512_1020	83356	0.57	0.57	0.40	0.40
20200513_0440	89187	0.75	0.75	0.41	0.41
20200513_1320	120552	1.46	1.46	0.55	0.55
20200514_1300	117080	1.28	1.28	0.39	0.39
20200517_1025	76730	0.89	0.89	0.38	0.38
20210105_1145	95261	0.96	2.04	0.54	0.34
20210110_0455	55329	1.91	3.33	0.58	0.40
20210110_1150	85402	0.88	1.64	0.57	0.40
20210112_0615	41136	0.79	1.99	0.61	0.44
20210112_0935	82254	0.79	1.50	0.64	0.48
20210113_1235	110113	1.85	0.47	0.56	0.36
20210517_1145	146941	0.72	1.48	0.66	0.51
20210617_1020	51520	1.00	1.88	0.56	0.38
20210617_1155	92144	1.17	2.15	0.61	0.45
20210618_1000	75992	1.64	0.86	0.59	0.42
20210619_0940	102514	0.90	1.01	0.57	0.38
20210621_0900	85251	1.44	0.76	0.56	0.38
20210621_1040	142265	1.61	0.86	0.58	0.41
20210622_0845	69095	1.18	1.06	0.57	0.39

V. CONCLUSION

Geolocation accuracy plays a vital role in applications of MERSI-II. In this study, we gave a brief view on the MERSI-II, which adopted 45° scanning mirrors to scan the earth, and a K-mirror to correct the image rotation. According to the optical design, a rigorous sensor model was developed to retrieve the imaging ray from the image coordinate to the ECEF coordinate. With exterior global DEM, the 3-D geodetic coordinate was determined to build the GLT. After compensating for attitude errors, the RMSEs of GLT which is built with design parameters, are approximately 0.52 pixels, achieving subpixel geolocation accuracy. However, there were systematic geolocation errors, relying on the view angles, frame numbers and line coordinates. The geolocation errors with large view angles were over 1 pixel, even with a larger GSD.

To further investigate the error properties, a homogenous coordinate frame in the focal plane was proposed. Errors caused by sensors, platforms, and targets were studied in such a frame. Despite the fact that as CCD position error in the flight direction introduces constant errors, the attitude compensation would cause the cosine curve errors when the pitch angle was adjusted to reduce the CCD position error. And there were scanning angle errors, perhaps introduced by mechanical scanning of 45° mirror. The alignment of the K-mirror should be modeled by rigorous sensor model

because the pitch angle of K-mirrors introduces oscillation errors of approximately 0.2 pixels between adjacent frames. The initial phase angle caused the residuals in image rotations, which change linearly with the line coordinate in the scanning direction. The principal distance errors would introduce linear errors with line coordinate in the flight direction. Principal distance correction was approximately $f/200$. After correcting all above errors, the systematic errors were removed and the RMSEs of 23 independent datasets achieved 0.4 pixels.

The systematic errors introduced by the initial phase angles and principal distance errors were rather small, approximately 0.1 pixels. This required highly accurate image matching. LSM can nevertheless achieve such accuracy in most cases. Many outliers were identified, which should be removed in future work. Limited by attitude accuracy of FY-3D OBC file, the geolocation accuracy can be further improved by other attitude records. The quaternions of FY-3D and FY-3E would be studied and integrated into automatic geometric calibration procedure for later.

Appendix A

A. Reflection Matrix

The reflected light ray r' is determined by the normal vector $\vec{n} = \begin{bmatrix} n_X & n_Y & n_Z \end{bmatrix}^T$ and incident ray r. According to the law of reflection, the r' is

$$r' = r - 2n \cdot \left(n^T \cdot r\right) = \left(I - 2n \cdot n^T\right) \cdot r = R_m \cdot r \quad (14)$$

where the reflection matrix R_m is

$$R_m = I - 2n \cdot n^T = \begin{bmatrix} 1 - 2n_X^2 & -2n_X n_Y & -2n_X n_Z \\ -2n_X n_Y & 1 - 2n_Y^2 & -2n_Y n_Z \\ -2n_X n_Z & -2n_Y n_Z & 1 - 2n_Z^2 \end{bmatrix}. \quad (15)$$

The 45° scanning mirror rotate θ about axis X, then the rotated normal vector is

$$n_\theta = R(\theta) \cdot n = \begin{bmatrix} 1 & 0 & 0 \\ 0 & \cos\theta & -\sin\theta \\ 0 & \sin\theta & \cos\theta \end{bmatrix} \cdot n. \quad (16)$$

The rotated reflection matrix $R_m(\theta)$ is

$$R_m(\theta) = R(\theta) \cdot R_m \cdot R^T(\theta). \quad (17)$$

In the case of K-mirror, the rotated reflected matrix $R_k(\theta/2)$ is composed by three rotated reflection matrices

$$\begin{aligned} R_k(\theta/2) &= R(\theta/2) \cdot R_{k_1} \cdot R^T(\theta/2) \cdot R(\theta/2) \cdot R_{k_2} \\ &\quad \cdot R^T(\theta/2) \cdot R(\theta/2) \cdot R_{k_3} \cdot R^T(\theta/2) \\ &= R(\theta/2) \cdot R_{k_1} \cdot R_{k_2} \cdot R_{k_3} \cdot R^T(\theta/2). \end{aligned} \quad (18)$$

When the 45° scanning mirror points to the nadir, the normal vectors of three reflectors are $\begin{bmatrix} \cos\beta & 0 & \sin\beta \end{bmatrix}^T$, $\begin{bmatrix} 0 & 0 & -1 \end{bmatrix}^T$ and $\begin{bmatrix} -\cos\beta & 0 & \sin\beta \end{bmatrix}^T$. According to (15) and (18), the reflection matrix of K-mirror is

$$R_{k0} = R_{k_1} \cdot R_{k_2} \cdot R_{k_3} = \begin{bmatrix} 1 & 0 & 0 \\ 0 & 1 & 0 \\ 0 & 0 & -1 \end{bmatrix}. \quad (19)$$

Appendix B

B. Boresight Misalignment of K-Mirror

The misalignment of K-mirror can be represented with three angles $\phi - \alpha - \gamma$. Then, the rotation matrix R_{ki} is defined as follows:

$$\begin{aligned} R_{ki} &= R_\phi \cdot R_\alpha \cdot R_\gamma \\ &= \begin{bmatrix} 1 & 0 & 0 \\ 0 & \cos\phi & -\sin\phi \\ 0 & \sin\phi & \cos\phi \end{bmatrix} \\ &\quad \cdot \begin{bmatrix} \cos\alpha & 0 & \sin\alpha \\ 0 & 1 & 0 \\ -\sin\alpha & 0 & \cos\alpha \end{bmatrix} \\ &\quad \cdot \begin{bmatrix} \cos\gamma & -\sin\gamma & 0 \\ \sin\gamma & \cos\gamma & 0 \\ 0 & 0 & 1 \end{bmatrix}. \end{aligned} \quad (20)$$

According to (18), the three reflectors can be rotated as a unit. In this case, the reflection matrix of K-mirror becomes

$$R_k = R_{\theta/2} \cdot R_{ki} \cdot R_{k0} \cdot R_{ki}^T \cdot R_{\theta/2}^T. \quad (21)$$

It is easy to prove that $R_\gamma \cdot R_{k0} \cdot R_\gamma^T = R_{k0}$, and $R_{\theta/2} \cdot R_\phi = R_{\theta/2+\phi}$. Therefore, the reflection matrix of K-mirror is as (22), shown at the bottom of the page.

Appendix C

C. Angle of 45° Scanning Mirror

If the scanning mirror is $45° + \tau$, the reflection matrix of 45° scanning mirror is

$$R_m = \begin{bmatrix} -\sin\tau & 0 & \cos\tau \\ 0 & 1 & 0 \\ \cos\tau & 0 & \sin\tau \end{bmatrix}. \quad (23)$$

Substitute (23) into (17), the rotated reflection matrix $R_m(\theta)$ is derived. Then we apply the rotated reflection matrix to (7) and (8), and the LoS in the body frame is

$$\begin{bmatrix} X \\ Y \\ Z \end{bmatrix}_b = \begin{bmatrix} 1 & 0 & 0 \\ 0 & \cos\theta & -\sin\theta \\ 0 & \sin\theta & \cos\theta \end{bmatrix} \cdot \begin{bmatrix} \cos\tau \cdot x + \sin\tau \cdot f \\ y \\ \sin\tau \cdot x - \cos\tau \cdot f \end{bmatrix}. \quad (24)$$

$$\begin{aligned} R_k &= R_{\theta/2+\phi} \cdot R_\alpha \cdot R_{k0} \cdot R_\alpha^T \cdot R_{\theta/2+\phi}^T \\ &= \begin{bmatrix} \cos 2\alpha & \sin 2\alpha \cdot \sin(\theta/2+\phi) & -\sin 2\alpha \cdot \cos(\theta/2+\phi) \\ \sin 2\alpha \cdot \sin(\theta/2+\phi) & 1 - 2\cos^2\alpha \cdot \sin^2(\theta/2+\phi) & \cos^2\alpha \cdot \sin(\theta+2\phi) \\ -\sin 2\alpha \cdot \cos(\theta/2+\phi) & \cos^2\alpha \cdot \sin(\theta+2\phi) & 1 - 2\cos^2\alpha \cdot \cos^2(\theta/2+\phi) \end{bmatrix} \end{aligned} \quad (22)$$

APPENDIX D

D. Attitude Errors

The attitudes of MERSI-II defined the transformation from the body system to orbit system. The three Euler angles φ, ω, κ, with *Y-Z-X* rotation order, were used to determine the rotation matrix

$$\begin{aligned} R_{\text{att}} &= R_\varphi \cdot R_\kappa \cdot R_\omega \\ &= \begin{bmatrix} \cos\varphi & 0 & -\sin\varphi \\ 0 & 1 & 0 \\ \sin\varphi & 0 & \cos\varphi \end{bmatrix} \\ &\quad \cdot \begin{bmatrix} \cos\kappa & -\sin\kappa & 0 \\ \sin\kappa & \cos\kappa & 0 \\ 0 & 0 & 1 \end{bmatrix} \\ &\quad \cdot \begin{bmatrix} 1 & 0 & 0 \\ 0 & \cos\omega & -\sin\omega \\ 0 & \sin\omega & \cos\omega \end{bmatrix}. \end{aligned} \tag{25}$$

The LoS in the body system, as defined in (8), is transformed to the orbit system with

$$\begin{bmatrix} X \\ Y \\ Z \end{bmatrix}_o = R_\varphi \cdot R_\kappa \cdot R_\omega \cdot R_{\text{mkt}} \cdot \begin{bmatrix} x \\ y \\ -f \end{bmatrix}. \tag{26}$$

Then, the LoS of the object can be transformed to the focal plane with

$$\begin{bmatrix} X \\ Y \\ Z \end{bmatrix}_c = R_{\text{mkt}}^{-1} \cdot R_\omega^{-1} \cdot R_\kappa^{-1} \cdot R_\varphi^{-1} \cdot \begin{bmatrix} X \\ Y \\ Z \end{bmatrix}_o. \tag{27}$$

The partial derivatives of $\begin{bmatrix} X_c & Y_c & Z_c \end{bmatrix}^T$ about φ, ω, κ can be calculated. In general, the orbit and attitude control system of FY-3D would maintain the body system aligning with orbit system. That is, $\varphi \approx 0, \omega \approx 0$ and $\kappa \approx 0$. Then, the partial derivatives are

$$\begin{aligned} \frac{\partial \begin{bmatrix} X & Y & Z \end{bmatrix}_c^T}{\partial \varphi} &= \begin{bmatrix} y \cdot \sin\theta - f \cdot \cos\theta \\ -x \cdot \sin\theta \\ -x \cdot \cos\theta \end{bmatrix} \\ \frac{\partial \begin{bmatrix} X & Y & Z \end{bmatrix}_c^T}{\partial \omega} &= \begin{bmatrix} 0 \\ -f \\ -y \end{bmatrix} \\ \frac{\partial \begin{bmatrix} X & Y & Z \end{bmatrix}_c^T}{\partial \kappa} &= \begin{bmatrix} y \cdot \cos\theta + f \cdot \sin\theta \\ -x \cdot \cos\theta \\ x \cdot \sin\theta \end{bmatrix}. \end{aligned}$$

According to the definition of homogenous coordinate (p_x, p_y), $(\Delta p_x, \Delta p_y)$ is calculated with

$$\begin{cases} \Delta p_x = \left(\dfrac{f}{\mu} + \dfrac{x^2}{\mu \cdot f}\right) \cdot \cos\theta \cdot \Delta\varphi - \left(\dfrac{f}{\mu} + \dfrac{x^2}{\mu \cdot f}\right) \\ \qquad \cdot \sin\theta \cdot \Delta\kappa \\ \Delta p_y = \dfrac{x}{\mu} \cdot \sin\theta \cdot \Delta\varphi + \dfrac{f}{\mu} \cdot \Delta\omega + \dfrac{x}{\mu} \cdot \cos\theta \cdot \Delta\kappa. \end{cases} \tag{28}$$

ACKNOWLEDGMENT

Hongbo Pan thanks Yong Yang at the Shanghai Academy of Spaceflight Technology for providing them with important information about the MERSI-II. The authors would like to thank the anonymous reviewers for their comments and constructive suggestions to improve the article.

REFERENCES

[1] M. Min *et al.*, "On-orbit spatial quality evaluation and image restoration of FengYun-3C/MERSI," *IEEE Trans. Geosci. Remote Sens.*, vol. 54, no. 12, pp. 6847–6858, Dec. 2016.
[2] Z. Yang, N. Lu, J. Shi, P. Zhang, C. Dong, and J. Yang, "Overview of FY-3 payload and ground application system," *IEEE Trans. Geosci. Remote Sens.*, vol. 50, no. 12, pp. 4846–4853, Dec. 2012.
[3] Z. Yang *et al.*, "Capability of FengYun-3D satellite in Earth system observation," *J. Meteorological Res.*, vol. 33, no. 6, pp. 1113–1130, Dec. 2019.
[4] N. Xu *et al.*, "Prelaunch calibration and radiometric performance of the advanced MERSI II on FengYun-3D," *IEEE Trans. Geosci. Remote Sens.*, vol. 56, no. 8, pp. 4866–4875, Aug. 2018.
[5] X. Dai and S. Khorram, "The effects of image misregistration on the accuracy of remotely sensed change detection," *IEEE Trans. Geosci. Remote Sens.*, vol. 36, no. 5, pp. 1566–1577, Sep. 1998.
[6] J. F. Moreno and J. Melia, "A method for accurate geometric correction of NOAA AVHRR HRPT data," *IEEE Trans. Geosci. Remote Sens.*, vol. 31, no. 1, pp. 204–226, Jan. 1993.
[7] G. W. Rosborough, D. G. Baldwin, and W. J. Emery, "Precise AVHRR image navigation," *IEEE Trans. Geosci. Remote Sens.*, vol. 32, no. 3, pp. 644–657, May 1994.
[8] G. Lin *et al.*, "Thirty-six combined years of MODIS geolocation trending," *Proc. SPIE*, vol. 11127, Sep. 2019, Art. no. 1112715.
[9] R. E. Wolfe *et al.*, "Achieving sub-pixel geolocation accuracy in support of MODIS land science," *Remote Sens. Environ.*, vol. 83, pp. 31–49, Nov. 2002.
[10] G. Lin and R. Wolfe, "JPSS-1/NOAA-20 VIIRS early on-orbit geometric performance," *Proc. SPIE*, vol. 10764, Sep. 2016, Art. no. 107641H.
[11] G. Lin *et al.*, "SNPP and NOAA-20 VIIRS on-orbit geolocation trending and improvements," *Proc. SPIE*, vol. 11501, Sep. 2020, Art. no. 1150112.
[12] R. E. Wolfe *et al.*, "Suomi NPP VIIRS prelaunch and on-orbit geometric calibration and characterization," *J. Geophys. Res., Atmos.*, vol. 118, no. 20, pp. 11508–11521, 2013.
[13] K. V. Khlopenkov, A. P. Trishchenko, and Y. Luo, "Achieving subpixel georeferencing accuracy in the Canadian AVHRR processing system," *IEEE Trans. Geosci. Remote Sens.*, vol. 48, no. 4, pp. 2150–2161, Apr. 2010.
[14] W. Li *et al.*, "A new geolocation error estimation method in MWRI data aboard FY3 series satellites," *IEEE Geosci. Remote Sens. Lett.*, vol. 17, no. 2, pp. 197–201, Feb. 2020.
[15] F. Tang, X. Zou, H. Yang, and F. Weng, "Estimation and correction of geolocation errors in FengYun-3C microwave radiation imager data," *IEEE Trans. Geosci. Remote Sens.*, vol. 54, no. 1, pp. 407–420, Jan. 2016.
[16] M. Guan and R. Wu, "Geolocation approach for FY-3A MERSI remote sensing image," *J. Appl. Meteorol. Sci.*, vol. 23, no. 5, p. 534, Oct. 2012.
[17] Z. Jing, S. Li, X. Hu, and F. Tang, "Sub-pixel accuracy evaluation of FY-3D MERSI-2 geolocation based on OLI reference imagery," *Int. J. Remote Sens.*, vol. 42, no. 19, pp. 7215–7238, Oct. 2021.
[18] S. Aksakal, C. Neuhaus, E. Baltsavias, and K. Schindler, "Geometric quality analysis of AVHRR orthoimages," *Remote Sens.*, vol. 7, no. 3, pp. 3293–3319, Mar. 2015.
[19] M. Schmidt, E. A. King, and T. R. McVicar, "Assessing the geometric accuracy of AVHRR data processed with a state vector based navigation system," *Can. J. Remote Sens.*, vol. 34, no. 5, pp. 496–508, Oct. 2008.
[20] M. Nishihama *et al.*, "MODIS level 1A Earth location: Algorithm theoretical basis document version 3.0," MODIS Science Data Support Team, Tech. Rep. SDST-092, 1997.
[21] M. Guan and Q. Guo, "Offsetting image rotation system in Fy-3 MERSI's geolocation," *J. Appl. Meteorol. Sci.*, vol. 19, no. 4, pp. 420–427, 2008.
[22] G. Petit and B. Luzum, *IERS Conventions (2010)*, vol. 36. Saint-Cloud, France: Bureau International des Poids et Mesures Sevres, 2010.

[23] J. J. Danielson and D. B. Gesch, "Global multi-resolution terrain elevation data 2010 (GMTED2010)," U.S. Dept. Interior, U.S. Geol. Surv., Washington, DC, USA, Tech. Rep. 2011-1073, 2011.
[24] H. Vermeille, "An analytical method to transform geocentric into geodetic coordinates," *J. Geodesy*, vol. 85, no. 2, pp. 105–117, Feb. 2011.
[25] T. Fukushima, "Transformation from Cartesian to geodetic coordinates accelerated by Halley's method," *J. Geodesy*, vol. 79, no. 12, pp. 689–693, Jan. 2006.
[26] T. Toutin, "Review article: Geometric processing of remote sensing images: Models, algorithms and methods," *Int. J. Remote Sens.*, vol. 25, no. 10, pp. 1893–1924, May 2004.
[27] P. Brunel and A. Marsouin, "Operational AVHRR navigation results," *Int. J. Remote Sens.*, vol. 21, no. 5, pp. 951–972, Jan. 2000.
[28] C. Bouzinac *et al.*, "Sentinel-2 level-1 calibration and validation status from the mission performance centre," in *Proc. IEEE Int. Geosci. Remote Sens. Symp.*, Jul. 2018, pp. 4347–4350.
[29] J. Ma, J. Jiang, H. Zhou, J. Zhao, and X. Guo, "Guided locality preserving feature matching for remote sensing image registration," *IEEE Trans. Geosci. Remote Sens.*, vol. 56, no. 8, pp. 4435–4447, Aug. 2018.

Hongbo Pan (Member, IEEE) received the B.E. and Ph.D. degrees in photogrammetry and remote sensing from Wuhan University, Wuhan, China, in 2009 and 2014, respectively.

He is currently an Associate Professor with the School of Geosciences and Info-Physics, Central South University, Changsha, China. His research interests include spaceborne photogrammetry and geometric processing of remote sensing imagery.

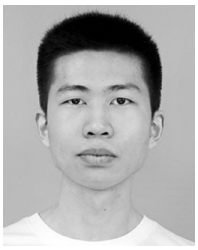

Zehua Cui is currently pursuing the master's degree with the School of Geosciences and Info-Physics, Central South University, Changsha, China.

His research interests are photogrammetry and remote sensing.

Xiuqing Hu received the B.Sc. degree in atmospheric science from Nanjing University, Nanjing, China, in 1996, the M.Sc. degree in cartography and geographical information systems from Beijing Normal University, Beijing, China, in 2004, and the Ph.D. degree in quantitative remote sensing science from the Institute of Remote Sensing Application, Chinese Academy of Sciences, Beijing, in 2012.

He is currently conducting research at the National Satellite Meteorological Center, China Meteorological Administration, Beijing. His research interests include calibration and validation for optical sensors, retrieval algorithms for aerosol/dust and water vapor, and climate data records from environment satellites.

Xiaoyong Zhu received the B.E. and master's degrees in photogrammetry and remote sensing from the School of Remote Sensing and Information Engineering, Wuhan University, Wuhan, China, in 2006 and 2008, respectively.

He is currently an Associate Researcher with the Land Satellite Remote Sensing Application Center, Ministry of Natural Resources, Beijing, China. His research interests include space photogrammetry and geometry processing of optical imagery.